arXiv:2504.09905v2 [eess.SP] 19 Apr 2025

Fusing Bluetooth with Pedestrian Dead Reckoning: A Floor Plan-Assisted Positioning Approach

Wenxuan Pan, Yang Yang, *Senior Member, IEEE*, Mingzhe Chen, *Senior Member, IEEE*, Dong Wei, Caili Guo, *Senior Member, IEEE*, and Shiwen Mao, *Fellow, IEEE*

***Abstract*—Floor plans can provide valuable prior information that helps enhance the accuracy of indoor positioning systems. However, existing research typically faces challenges in efficiently leveraging floor plan information and applying it to complex indoor layouts. To fully exploit information from floor plans for positioning, we propose a floor plan-assisted fusion positioning algorithm (FP-BP) using Bluetooth low energy (BLE) and pedestrian dead reckoning (PDR). In the considered system, a user holding a smartphone walks through a positioning area with BLE beacons installed on the ceiling, and can locate himself in real time. In particular, FP-BP consists of two phases. In the offline phase, FP-BP programmatically extracts map features from a stylized floor plan based on their binary masks, and constructs a mapping function to identify the corresponding map feature of any given position on the map. In the online phase, FP-BP continuously computes BLE positions and PDR results from BLE signals and smartphone sensors, where a novel grid-based maximum likelihood estimation (GML) algorithm is introduced to enhance BLE positioning. Then, a particle filter is used to fuse them and obtain an initial estimate. Finally, FP-BP performs post-position correction to obtain the final position based on its specific map feature. Experimental results show that FP-BP can achieve a real-time mean positioning accuracy of 1.19 m, representing an improvement of over 28% compared to existing floor plan-fused baseline algorithms.**

***Index Terms*—Bluetooth low energy (BLE), floor plan constraints, fusion positioning, pedestrian dead reckoning (PDR)**

I. Introduction

With the wide adoption of emerging applications such as smart cities, Industry 4.0, and extended reality (XR), the need for accurate indoor positioning has become more critical than ever. Although the global navigation satellite system (GNSS) has demonstrated high accuracy and wide coverage in outdoor scenarios, it still faces challenges in indoor applications, due to the weak satellite signals and environmental obstructions [2], [3]. To address these challenges, various indoor positioning technologies, such as WiFi [4], Bluetooth low energy (BLE) [5], radio frequency identification (RFID) [6], visible light positioning (VLP) [7], and ultra-wideband (UWB) [8], have been proposed. Among these, BLE positioning stands out due to its advantages of low cost and high energy efficiency [9].

BLE positioning typically uses the received signal strength indicator (RSSI) as the primary measurement, deriving common algorithms such as trilateration [10] and fingerprinting [11], [12]. The ease of obtaining BLE RSSIs has facilitated the widespread adoption of RSSI-based algorithms in BLE positioning. However, due to the complexity of indoor environments, the BLE RSSI is affected by environmental variations and interference, resulting in significant fluctuations, limiting RSSI-based BLE positioning to meter-level accuracy [13], [14]. Since Bluetooth 5.1 [15], the Bluetooth Special Interest Group (SIG) has introduced new positioning methods based on the angle of arrival (AoA) or angle of departure (AoD). Although AoA/AoD-based algorithms have demonstrated higher accuracy than those based on RSSI in general [2], the additional multi-antenna hardware requirements also lead to increased positioning costs [16]. More importantly, common devices, such as smartphones, are equipped with only one single Bluetooth antenna, which makes AoA/AoD-based algorithms inapplicable. Therefore, RSSI-based algorithms remain the most widely used in BLE positioning [17].

To improve the positioning accuracy of BLE, some fusion-based positioning technologies have been proposed. Among these, pedestrian dead reckoning (PDR) has emerged as a popular method [18]. Note that PDR typically comprises an inertial measurement unit (IMU) consisting of an accelerometer and a gyroscope, a magnetometer, and other sensors, and thus it can provide abundant extra information, such as movement speed and direction, over short periods. However, PDR-based positioning requires an accurate initial position and suffers from significant accuracy degradation over time due to cumulative errors of PDR [18], [19]. By integrating other positioning methods such as BLE, these errors can be effectively mitigated [13]. In particular, the absolute position references provided by BLE can help correct the PDR cumulative errors, and thus enhance the overall reliability of the fusion system.

Due to the lack of indoor layout information, traditional algorithms inevitably yield results that appear in undesirable

Manuscript received April 19, 2021; revised August 16, 2021. This work is supported, in part by the BUPT Innovation and Entrepreneurship Support Program under Grant 2025-YC-S007. An earlier version [1] of this paper has been accepted by the 2025 IEEE International Conference on Communications Workshops (ICC Workshops). *(Corresponding author: Yang Yang.)*

Wenxuan Pan and Yang Yang are with Beijing Key Laboratory of Network System Architecture and Convergence, School of Information and Communication Engineering, Beijing University of Posts and Telecommunications, Beijing 100876, China (e-mail: pwx@bupt.edu.cn; yangyang01@bupt.edu.cn).

Mingzhe Chen is with the Department of Electrical and Computer Engineering and the Institute for Data Science and Computing, University of Miami, Coral Gables, FL 33146 USA (e-mail: mingzhe.chen@miami.edu).

Dong Wei is with the Institute of Information Engineering, Chinese Academy of Sciences, Beijing 100093, China (e-mail: weidong@iie.ac.cn).

Caili Guo is with Beijing Laboratory of Advanced Information Networks, School of Information and Communication Engineering, Beijing University of Posts and Telecommunications, Beijing 100876, China (e-mail: guocaili@bupt.edu.cn).

Shiwen Mao is with the Wireless Engineering Research and Education Center, Auburn University, Auburn, AL 36849 USA (e-mail: smao@ieee.org).

0000–0000/00$00.00 © 2021 IEEE

areas [20], such as inside obstacles or cross walls, which compromises their system stability. Under this background, the integration of floor plans as extra prior information, has shown potential. The floor plan can provide serious restrictions of the indoor environment [20], [21], making floor plan-integration a promising direction for advancing fusion-based positioning algorithms.

A. Related Works

Current studies on fusing BLE/WiFi with PDR can be categorized into two types: (i) Calculate the BLE/WiFi positioning results first, typically through methods like trilateration [22], [23] or fingerprinting [20], [24], and then fuse these results with PDR; (ii) Fuse the received BLE/WiFi data, such as BLE RSSI or WiFi round-trip time (RTT), with IMU data directly [25]. For instance, Kong *et al.* [26] directly used an adaptive feedback extended Kalman filter (EKF) to fuse beacon positions, received RSSIs, and the result of PDR, to enhance the accuracy of the estimated position. In terms of filtering mechanisms, the above algorithms commonly employ the Kalman filter (KF) [22], [23] or its extended variations, such as the EKF [24], [26], as well as the particle filter (PF) [20]. However, none of the above traditional algorithms consider the integration of floor plans, which contain useful information such as environmental restrictions and pedestrian accessibility for positioning.

To further take the environmental factors into consideration, integrating floor plans in positioning systems has become a research hotspot [21], [27], [28], [29]. In general, the floor plan can also be regarded as a type of sensor [13]. In indoor positioning scenarios, floor plans are readily available [27] and can effectively constrain positioning results to the walkable area, thereby improving positioning performance [30], [31]. With respect to the filtering mechanisms, the PF is considered highly compatible with map information [21]. As such, many floor plan-integrated algorithms adopt PF for fusion. In [32], the authors generate particles in PF based on a specific angular probability density function (PDF), effectively avoiding "wall-crossing" particles. However, this algorithm requires frequent and extensive wall-distance checks, resulting in high computational costs in practical scenarios. The authors in [33] directly assign zero weights to "wall-crossing" particles in PF. Similarly, in [34], the authors use the map to remove particles that fall outside the map boundaries. However, these algorithms [33], [34] only simply eliminate particles in a position with large deviations, and this may lead to particle depletion and even positioning failure. The authors in [35] use changes in gyroscope yaws to determine whether the user has reached a corner, and thus can identify the corner and correct the yaw. However, this algorithm requires the pre-establishment of corner and fingerprint databases, which increases the offline workload. Although interesting, the above algorithms [33], [34], [35] have not fully utilized the floor plan information, such as the constraints of different obstacles, and therefore cannot provide stable positioning or require additional work.

To extract more floor plan information (e.g. wall/corridor directions) for positioning, the authors in [36] assume walls are straight lines and determine "wall-crossing" by checking for intersections between particle movement and walls. Wang *et al.* [37] assume the angles of corners are all right angles, with straight paths between every two adjacent corners. Similarly, Choi *et al.* [38] also assume corridors as vertical or horizontal segments, and build a virtual graph to correct the user's position and orientation to the door when detecting a "door-crossing" event. Du *et al.* [20] proposed an automatic map preprocessing method and an enhanced PF algorithm that integrates a floor plan based on image processing for line detection. However, the above algorithms [20], [36], [37], [38] require the floor plan to exhibit regularly, such as straight corridors with distinct directional changes. This leads to a limitation on map geometry, making them unsuitable for complex floor plans and indoor layouts.

Although the above algorithms [20], [32], [33], [34], [35], [36], [37] and [38] have integrated floor plans, they struggle to fully utilize map information or adapt to complex indoor layouts, particularly when extracting map feature boundaries and leveraging their constraints in irregular environments. This may limit the feasibility and accuracy, or increase the deployment cost of the system in real-world scenarios. Thereby, a general and efficient floor plan-assisted fusion positioning algorithm deserves further investigation.

B. Contributions

The main contribution of this paper is a novel floor plan-assited real-time fusion positioning system. To the authors' best knowledge, this is *the first fusion framework that integrates a floor plan to achieve accurate real-time positioning without any limitations on map geometry.*[1] Our key contributions are summarized as follows:

- We propose a floor plan-assisted fusion positioning algorithm using BLE and PDR (FP-BP). When positioning, FP-BP fuses the BLE position and PDR through PF to obtain an initial result. Then, a post-position correction (PPC) algorithm is proposed to integrate the floor plan deeply into the system, using the map constructed from the floor plan in advance. It determines whether the initial result needs to be corrected by floor plan constraints, and applies corrections based on different map features to obtain the final position.
- To programmatically build maps from various floor plans, we propose a feature extraction-based mapping method. This method first standardizes the floor plan style by filtering different obstacle areas and filling them with specific colors. Next, a binary mask-based method is applied to extract the inner contours of the floor plan. Finally, we establish coordinate systems on the floor plan and define a map feature function. This preprocessing mapping method can be completed in advance during the offline phase, and is widely applicable to various floor plans without any restriction.

[1]Based on the preliminary version [1] of this work, an enhanced BLE positioning algorithm named GML is proposed in this paper for the first time. Moreover, based on the proposed FP-BP algorithm, a prototype is developed for real-time positioning on mobile devices.

- To further enhance the accuracy of BLE positioning in FP-BP, we propose a grid-based maximum likelihood estimation (GML) algorithm. By analyzing the PDF of RSSI-estimated distance, we construct a likelihood function based on maximum likelihood estimation (MLE). Maximizing this likelihood function, the algorithm selects the optimal grid point within a virtual grid array as the estimated result, accommodating both dense and sparse beacon deployment scenarios. Finally, we apply mean filtering to multiple historical results to improve stability and accuracy.

Experimental results show that FP-BP algorithm can achieve a mean positioning accuracy of 1.19 m, which is improved by over 28% compared to existing floor plan-fused baselines. In addition, the proposed GML algorithm also reaches a mean accuracy of 2.01 m when the user keeps moving, which outperforms existing baselines by over 21%.

C. Notations and Paper Organization

We adopt the following notations: Matrices are denoted by uppercase boldface such as $\boldsymbol{R}$; Points and column vectors are denoted by lowercase boldface such as $\boldsymbol{v}$; $\boldsymbol{v}^{\mathsf{T}}$ and $\|\boldsymbol{v}\|$ represent the transposition and the norm of vector $\boldsymbol{v}$, respectively; Sets are denoted by calligraphic characters such as $\mathcal{A}$; $\{a_i\}_{i=1}^{n}$ represents a sequence containing n elements and is arranged in order; $\mathcal{N}(\mu, \sigma^2)$ represents a Gaussian distribution with an expectation of μ and a variance of σ^2; $p(\boldsymbol{x}|\boldsymbol{y})$ represents the PDF of a random variable $\boldsymbol{x}$ given the condition $\boldsymbol{y}$; and $\mathbb{E}_{\boldsymbol{x}|\boldsymbol{y}}[\boldsymbol{z}]$ denotes the expectation of a random variable $\boldsymbol{z} = \boldsymbol{z}(\boldsymbol{x})$ under the PDF $p(\boldsymbol{x}|\boldsymbol{y})$.

The rest of the paper is organized as follows. Section II shows the system model. The proposed GML and FP-BP algorithms are introduced in Sections III and IV, respectively. Then, Section V presents the experimental setup and results of the proposed positioning system. Finally, we conclude this paper in Section VI.

II. System Model and Problem Formulation

A. System Model

This section considers a typical positioning scenario as illustrated in Fig. 1, where a pedestrian carrying a smartphone passes through an indoor area and receives signals from BLE beacons for positioning. The beacons broadcast BLE signals at a fixed frequency, and the smartphone, i.e. the receiver, continuously scans for these signals. The smartphone also listens to the built-in sensors to obtain the user motion data, which is then fused with the BLE estimated position and the preprocessed floor plan information, allowing the user to locate himself in real time.

The overall architecture of FP-BP is shown in Fig. 2. The FP-BP consists of an offline and an online phase. In particular, the online phase of FP-BP further consists of two modules:

1) BLE Positioning: When the smartphone scans for BLE signals, it can obtain information such as the universally unique identifier (UUID) and the instant RSSI of a beacon. The path loss of RSSI can be modeled as [13], [33], [34]:

$$R = -10n \log d + R_0 + X(\sigma), \tag{1}$$

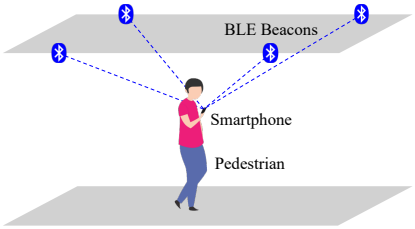

Fig. 1: Scenario of the considered system.

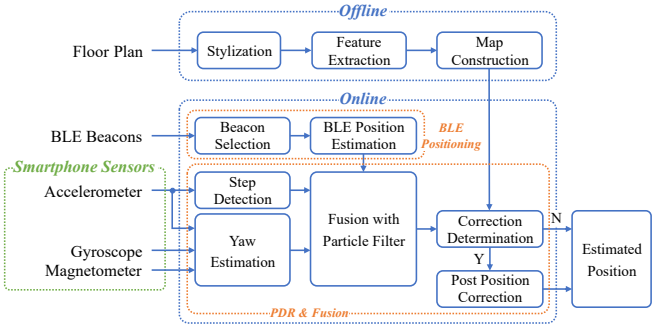

Fig. 2: Overall architecture of FP-BP.

where R is the measured RSSI in dBm; n is the loss factor; R_0 is the RSSI at a distance of 1 m, and $X(\sigma) \sim \mathcal{N}(0, \sigma^2)$ is a zero-mean Gaussian noise. Let $\mathcal{B}$ be the set of beacons' positions and $\mathcal{R}$ be the set of received RSSIs. Then, BLE positioning can be expressed as:

$$\boldsymbol{x}_B = \boldsymbol{f}_{BLE}(\mathcal{R}, \mathcal{B}), \tag{2}$$

where $\boldsymbol{x}_B$ is the estimated position of the user from BLE positioning systems. In particular, we apply the GML algorithm at a fixed time interval in the *BLE Positioning* module to compute and store the current BLE position. This process will be detailed in Section III.

2) PDR&Fusion: The smartphone can obtain data from built-in sensors at a fixed frequency for step detection and yaw estimation. Assume the instant sensor data is $\mathcal{D}_s$, and then the position update based on PDR is expressed as:

$$\boldsymbol{x}_P = \boldsymbol{x}^- + \boldsymbol{f}_{PDR}(\mathcal{D}_s) \triangleq \boldsymbol{x}^- + \boldsymbol{s}, \tag{3}$$

where $\boldsymbol{x}_P$ is the estimated position of PDR, and $\boldsymbol{x}^-$ is the positioning result at the previous moment. Upon detecting a step event, i.e., $\|\boldsymbol{s}\| > 0$, the *PDR&Fusion* module fuses the step $\boldsymbol{s}$ with the stored BLE position using PF algorithm to obtain the initial estimated position.

Finally, floor plan integration is performed. In the offline phase, floor plan preprocessing has enabled the extraction of the set of points in walkable area, $\mathcal{W}$, from the set of the entire map area, $\mathcal{M}$, in advance. Let the current estimated position be $\widehat{\boldsymbol{x}}$. When users walk indoors, they can only move from one walkable position to another, with no obstacles blocking the path. Therefore, we apply the floor plan constraint by ensuring $\boldsymbol{x}^-$, $\widehat{\boldsymbol{x}}$, and all points between these two estimated positions remain within walkable area:

$$(1-\lambda)\boldsymbol{x}^- + \lambda\widehat{\boldsymbol{x}} \in \mathcal{W}, \ \forall \lambda \in [0, 1]. \tag{4}$$

In particular, we apply the proposed PPC algorithm to determine and perform necessary correction, and output the final position. This process will be detailed in Section IV.

B. Problem Formulation

The target of this paper is to locate the user based on the BLE estimation in (2), PDR prediction in (3), and floor plan constraint (4). Taking the BLE estimation $\boldsymbol{x}_B$ as the current observation, then according to Bayes' theorem, given all observations $\mathcal{Z}$ including $\boldsymbol{x}_B$, the posterior PDF of current position $\boldsymbol{x}$ is calculated as [39]:

$$p(\boldsymbol{x}|\mathcal{Z}) = \frac{p(\boldsymbol{x}_B|\boldsymbol{x}) \cdot p(\boldsymbol{x}|\mathcal{Z}^-)}{p(\boldsymbol{x}_B|\mathcal{Z}^-)}, \tag{5}$$

where $p(\boldsymbol{x}_B|\boldsymbol{x})$ is the likelihood; $p(\boldsymbol{x}|\mathcal{Z}^-)$ is the prior PDF based on the state transition model; and $p(\boldsymbol{x}_B|\mathcal{Z}^-)$ is a normalization constant independent of $\boldsymbol{x}$. Note that $\mathcal{Z}^-$ represents all historical observations, and $\mathcal{Z}$ represents all available observations including $\boldsymbol{x}_B$, i.e., $p(\boldsymbol{x}|\mathcal{Z}) = p(\boldsymbol{x}|\{\mathcal{Z}^-, \boldsymbol{x}_B\})$. Although the PDR prediction is not explicitly reflected in (5), it is closely related to $p(\boldsymbol{x}|\mathcal{Z}^-)$, which is calculated as:

$$p(\boldsymbol{x}|\mathcal{Z}^-) = \int_{\mathcal{M}} p(\boldsymbol{x}|\boldsymbol{x}^-)p(\boldsymbol{x}^-|\mathcal{Z}^-)\mathrm{d}\boldsymbol{x}^-. \tag{6}$$

In (6), the PDF of the state transition model, $p(\boldsymbol{x}|\boldsymbol{x}^-)$, is determined by the PDR prediction.

According to the minimum mean square error (MMSE) principle and constraint (4), we minimize the MSE between the true position $\boldsymbol{x}$ and the estimated position $\widehat{\boldsymbol{x}}$ by:

$$\min_{\widehat{\boldsymbol{x}}} \ \mathbb{E}_{\boldsymbol{x}|\mathcal{Z}}[(\boldsymbol{x} - \widehat{\boldsymbol{x}})^2] \ \text{ s.t. } (4). \tag{7}$$

If we neglect constraint (4), let $\mathrm{d}\mathbb{E}_{\boldsymbol{x}|\mathcal{Z}}[(\boldsymbol{x} - \widehat{\boldsymbol{x}})^2]/\mathrm{d}\widehat{\boldsymbol{x}} = 0$ in (7), and then we can obtain the optimal estimation $\widehat{\boldsymbol{x}}^*$ by:

$$\widehat{\boldsymbol{x}}^* = \mathbb{E}_{\boldsymbol{x}|\mathcal{Z}}[\boldsymbol{x}] = \int_{\mathcal{M}} \boldsymbol{x} \cdot p(\boldsymbol{x}|\mathcal{Z})\mathrm{d}\boldsymbol{x}. \tag{8}$$

However, considering the complexity of PDF $p(\boldsymbol{x}|\mathcal{Z})$ and the irregularity of area $\mathcal{W}$, problem (7) does not admit a closed-form solution generally. Although methods such as PF (see Section IV-C) can approximate the numerical solution to (8), they still struggle to satisfy constraint (4). To effectively extract the $\mathcal{W}$ area and incorporate floor plan constraints, we will detail the proposed algorithm in the following sections.

III. GML Algorithm for BLE Positioning

In this section, we propose the GML algorithm based on the MLE principle, to estimate the BLE positioning result $\boldsymbol{x}_B$. Assume there are N' beacons distributed in the positioning area, with their map coordinates be $\boldsymbol{b}_i \in \mathcal{B}$, $i = 1, 2, \ldots, N'$. The GML algorithm first selects $N \geq 3$ beacons with the largest RSSIs for positioning [40]. Suppose the set of selected beacons is:

$$\mathcal{B}_N = \{\boldsymbol{b}^{(1)}, \boldsymbol{b}^{(2)}, \ldots, \boldsymbol{b}^{(N)}\} \subset \mathcal{B}, \tag{9}$$

where the map coordinate of the i-th beacon is $\boldsymbol{b}^{(i)} = [x_i, y_i]^\mathsf{T}$. Let the RSSI received from $\boldsymbol{b}^{(i)}$ after Kalman filtering be denoted as $\widehat{R}_i$. According to (1), $\widehat{R}_i$ still follows a Gaussian distribution with its variance denoted as $\widehat{\sigma}_i^2$, giving:

$$\widehat{R}_i = -10n \log d_i + R_0 + X(\widehat{\sigma}_i) \tag{10a}$$

$$= -10n \log \widehat{d}_i + R_0, \tag{10b}$$

where d_i and $\widehat{d}_i$ are the true and estimated distances, respectively. From (10a) and (10b), we obtain:

$$\log \widehat{d}_i = \frac{X(\widehat{\sigma}_i)}{10n} + \log d_i \sim \mathcal{N}\left(\log d_i, \frac{\widehat{\sigma}_i^2}{(10n)^2}\right), \tag{11}$$

which indicates that $\log \widehat{d}_i$ still follows a Gaussian distribution. If we define

$$\begin{cases} \mu_i \triangleq \log d_i, \\ \eta_i^2 \triangleq \widehat{\sigma}_i^2/(10n)^2, \end{cases} \tag{12}$$

then $\widehat{d}_i$ follows a Log-Gaussian distribution with base 10 and parameters (μ_i, η_i^2), which can be expressed as:

$$\widehat{d}_i \sim \mathcal{LN}_{10}(\mu_i, \eta_i^2), \tag{13}$$

and the posterior PDF of $\widehat{d}_i$ is:

$$p(\widehat{d}_i|\boldsymbol{y}) = \frac{1}{\sqrt{2\pi\eta_i^2}\widehat{d}_i \ln 10} \exp\left[-\frac{(\log \widehat{d}_i - \mu_i)^2}{2\eta_i^2}\right]. \tag{14}$$

The expectation of $\widehat{d}_i$ can be then calculated as:

$$\mathbb{E}_{\widehat{d}_i|\boldsymbol{y}}[\widehat{d}_i] = \int_0^{+\infty} \widehat{d}_i p(\widehat{d}_i|\boldsymbol{y}) \ \mathrm{d}\widehat{d}_i = 10^{\mu_i + \frac{\eta_i^2}{2}\ln 10}. \tag{15}$$

Substituting (12) into (15), we obtain:

$$\mathbb{E}_{\widehat{d}_i|\boldsymbol{y}}[\widehat{d}_i] = d_i \cdot \exp\left[\frac{1}{2}\left(\frac{\widehat{\sigma}_i \ln 10}{10n}\right)^2\right], \tag{16}$$

which indicates that the expected estimated distance $\widehat{d}_i$ deviates from the real distance d_i due to the presence of noise. To mitigate this impact, GML algorithm does not directly use $\widehat{d}_i$ as the true distance in calculations. Instead, it considers from the perspective of posterior PDF $p(\widehat{d}_i|\boldsymbol{y})$. Let the likelihood function of a point $\boldsymbol{y}$ with respect to all beacons in $\mathcal{B}_N$ be:

$$\ell(\boldsymbol{y}) = \prod_{i=1}^{N} p(\widehat{d}_i|\boldsymbol{y}). \tag{17}$$

Taking the logarithm on both sides of (17) yields:

$$\ln \ell(\boldsymbol{y}) = -\sum_{i=1}^{N}\left[\frac{1}{2\eta_i^2}(\log \widehat{d}_i - \mu_i)^2\right] + c, \tag{18}$$

where c is a constant independent of $\boldsymbol{y}$. According to the MLE principle, the optimal estimated position $\boldsymbol{y}^*$ is determined by maximizing the $\ln \ell(\boldsymbol{y})$, which is equivalent to:

$$\boldsymbol{y}^* = \arg\min_{\boldsymbol{y}\in\mathcal{G}'} \sum_{i=1}^{N} \frac{1}{2\eta_i^2}\left(\log \widehat{d}_i - \log \|\boldsymbol{y} - \boldsymbol{b}^{(i)}\|\right)^2, \tag{19}$$

where $\mathcal{G}'$ is the set of candidate points. Generally, (19) is a nonlinear optimization problem that is challenging to solve. We construct a set of grid points distributed throughout the entire area (see Section IV-A4), denoted as $\mathcal{G}$, and transform

(19) into a problem of selecting an optimal point within a discrete grid point set $\mathcal{G}' \subset \mathcal{G}$. Let $\text{int}\mathcal{C}_N$ be the interior area of the convex hull $\mathcal{C}_N = \mathcal{CH}(\mathcal{B}_N)$ [41] formed by all beacons in $\mathcal{B}_N$, and $d(\boldsymbol{y}_1, \boldsymbol{y}_2)$ denote the Manhattan distance between point $\boldsymbol{y}_1$ and $\boldsymbol{y}_2$. When beacons are densely deployed in the positioning area, we can assume that the user's position is always within $\text{int}\mathcal{C}_N$, then the candidate grid points should also be close to the previous position $\boldsymbol{x}^{(k-1)}$:

$$\mathcal{G}'_1 = \{\boldsymbol{y} \mid \boldsymbol{y} \in (\mathcal{G} \cap \text{int}\mathcal{C}_N) \wedge d(\boldsymbol{y}, \boldsymbol{x}^{(k-1)}) < d_0\}. \quad (20)$$

In this way, we can effectively reduce the time delay caused by searching through a large number of grid points in $\mathcal{G}$.

If the beacons are deployed sparsely, i.e., the $\text{int}\mathcal{CH}(\mathcal{B})$ cannot geometrically cover the entire positioning area, the candidate grid points should not be restricted inside $\text{int}\mathcal{C}_N$. In this case, $\mathcal{G}'$ is represented as:

$$\mathcal{G}'_2 = \{\boldsymbol{y} \mid \boldsymbol{y} \in \mathcal{G} \wedge d(\boldsymbol{y}, \boldsymbol{x}^{(k-1)}) < d_0\}. \quad (21)$$

In the experimental scenario of this paper, $\mathcal{G}'_1$ is taken as the candidate grid points set. For simplicity, it is assumed that the η_i of all beacons are equal. The BLE positioning result at current time t is obtained by averaging $\boldsymbol{y}^*$ and the previous $(n-1)$ BLE positioning results:

$$\boldsymbol{x}_B^{(t)} = \frac{1}{n}\left(\boldsymbol{y}^* + \sum_{i=1}^{n-1} \boldsymbol{x}_B^{(t-i)}\right). \quad (22)$$

From the above analysis, it is evident that GML algorithm takes the RSSI noise into consideration, and uses the posterior PDF of $\widehat{d}_i$ to form a unique likelihood, thereby reducing errors. To fuse BLE results into our positioning system, we will detail the proposed FP-BP algorithm in the following section.

IV. FP-BP Algorithm

This section proposes the FP-BP algorithm, which consists of four steps: (i) preprocessing the floor plan, (ii) obtaining the PDR result, (iii) fusing BLE with PDR, and (iv) performing necessary PPC based on the floor plan.

A. Floor Plan Preprocessing

To deeply integrate floor plans into the positioning system, preprocessing should be carried out in advance. The main steps of preprocessing include stylization, feature extraction, and map construction.

1) Stylization: To eliminate the distractions of engineering drawings, we redraw a stylized floor plan for positioning. In particular, the floor plan map features required by the algorithm often include *Wall* (i.e. non-passable obstacles) and *Door* (i.e. conditionally passable obstacles). We use distinguishable colors to fill the *Wall* and *Door* areas, such as black and red, while the *Walkable* areas are filled with white, as illustrated in Fig. 3(a).

2) Feature Extraction: To identify the *Rooms* and obtain the precise areas of different map features, we need to extract these features from the floor plan. A mask-based method simplifies this process effectively. Adding the binary masks [42] of *Walls*, $\boldsymbol{I}_{Wall}$, and *Doors*, $\boldsymbol{I}_{Door}$, we obtain the mask of the whole

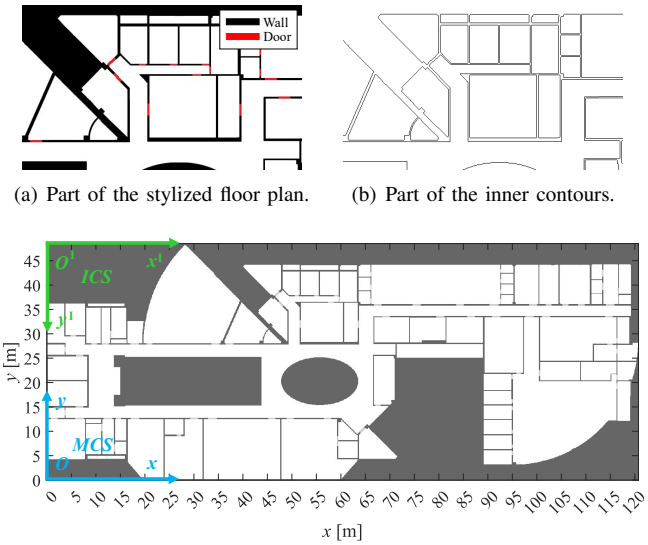

(a) Part of the stylized floor plan. (b) Part of the inner contours.

(c) Processed map $\boldsymbol{M}(\boldsymbol{x})$.

Fig. 3: Offline preprocessing of the experimental area floor plan.

obstacle area $\boldsymbol{I}_{obs}$ by $\boldsymbol{I}_{obs} = \boldsymbol{I}_{Wall} + \boldsymbol{I}_{Door}$. Then, we extract the inner contours of $\boldsymbol{I}_{obs}$, which represent either a *Room* or an obstacle boundary within the *Room*, as shown in Fig. 3(b).

3) Map Construction: To efficiently integrate the floor plan into the positioning algorithm, two coordinate systems are defined on the floor plan image: the map coordinate system (MCS) and the image coordinate system (ICS), as shown in Fig. 3(c). The transformation between ICS and MCS is:

$$\begin{bmatrix} x \\ y \end{bmatrix} = \frac{1}{r}\begin{bmatrix} x^{\text{I}} \\ H^{\text{I}} - y^{\text{I}} \end{bmatrix}, \quad (23)$$

where $\boldsymbol{x} = [x, y]^{\text{T}}$ and $\boldsymbol{x}^{\text{I}} = [x^{\text{I}}, y^{\text{I}}]^{\text{T}}$ are the map coordinate and image coordinate respectively; r is the resolution factor that represents the number of pixels in ICS corresponding to a distance of 1 m in MCS, and H^{I} is the height of the floor plan image in pixels.

For a given point in MCS, we need to obtain its map feature to determine which area the point is in, including *Walkable*, *Wall*, and *Door* areas. This allows us to correct the coordinates of this point based on its map feature. Based on the MCS, we define a map feature function $\boldsymbol{M}(\boldsymbol{x}) = \boldsymbol{I}(\boldsymbol{x}^{\text{I}}) \in [0, 1]$, where:

$$\boldsymbol{I}(\boldsymbol{x}^{\text{I}}) = \boldsymbol{I}_{Wall}(\boldsymbol{x}^{\text{I}}) + 0.5\boldsymbol{I}_{Door}(\boldsymbol{x}^{\text{I}}). \quad (24)$$

For a point $\boldsymbol{x}$ in the MCS, querying $\boldsymbol{M}(\boldsymbol{x})$ determines the map feature to which the point $\boldsymbol{x}$ belongs:

$$\boldsymbol{M}(\boldsymbol{x}) = \begin{cases} 0, & \boldsymbol{x} \textit{ is } \textbf{\textit{Walkable}}, \\ 0.5, & \boldsymbol{x} \textit{ is } \textbf{\textit{Door}}, \\ 1, & \boldsymbol{x} \textit{ is } \textbf{\textit{Wall}}. \end{cases} \quad (25)$$

The role of the floor plan is to restrict the estimated position $\boldsymbol{x}$ within the *Walkable* area $\mathcal{W} = \{\boldsymbol{x} \mid \boldsymbol{M}(\boldsymbol{x}) = 0\}$, since it is generally unrealistic for pedestrians to walk or remain in obstacle areas. Note that in the following text, we will abbreviate this map feature function as the *map*.

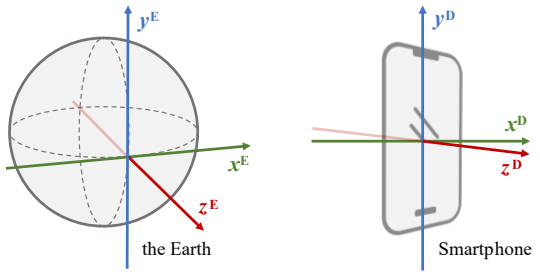

(a) The ECS. (b) The DCS.

Fig. 4: The defined 3-D ECS and DCS [43].

4) Grid Array Construction: In Section III, we have proposed the GML algorithm, which selects the grid point with the maximum likelihood probability as the positioning result. To apply the GML algorithm for BLE positioning, we need to construct a virtual grid array in advance, where the grid points are distributed over the entire map. Also, we should remove all the grid points within obstacle areas. Let the map range be $[0, X] \times [0, Y]$, and the grid interval be I_M. Then, the position of the (i, j)-th grid point is $\boldsymbol{g}_{ij} = [(i + 0.5)X/I_M, (j + 0.5)Y/I_M]^{\mathsf{T}}$, where $1 \le i \le \lfloor X/I_M \rfloor - 1$, $1 \le j \le \lfloor Y/I_M \rfloor - 1$, and $\lfloor \cdot \rfloor$ denotes the floor function. Let the grid array be denoted as $\mathcal{G}$, and then all grid points in $\mathcal{G}$ are located in *Walkable* area, i.e., $\mathcal{G} = \{\boldsymbol{g}_{ij} \mid \boldsymbol{M}(\boldsymbol{g}_{ij}) = 0\}$. Substituting this grid array $\mathcal{G}$ into (20) and (21), we can ensure that the BLE estimation result is located solely within *Walkable* area.

All of the above steps can be completed during the offline phase. Additionally, downsampling can be performed before stylization when the size of the floor plan is too large. This is because a large floor plan will lead to a large resolution factor r. Although this results in a higher map resolution, it also leads to larger computational costs. Therefore, it is necessary to downsample the floor plan, and set r to an appropriate value without affecting the poisitioning accuarcy.

B. Pedestrian Dead Reckoning (PDR)

In this subsection, the following coordinate systems are first defined: (i) the east-north-up coordinate system (ECS), whose axes are parallel to the east, north, and upward directions, as shown in Fig. 4(a); (ii) the device coordinate system (DCS), which is defined by the Android Developers [43] as shown in Fig. 4(b); (iii) the 3-dimensional (3-D) MCS, where the xy-plane is the same as that of the 2-D MCS in Section IV-A3, and the z-axis is determined by the cross product of the x- and y-axes. In reality, the z-axis of 3-D MCS is considered aligned with that of ECS.

The rotation from DCS to ECS is typically obtained in the form of quaternions from the gyroscope, denoted as $\boldsymbol{q}_{\mathrm{D}}^{\mathrm{E}} = q_x \mathrm{i} + q_y \mathrm{j} + q_z \mathrm{k} + q_w$. By converting $\boldsymbol{q}_{\mathrm{D}}^{\mathrm{E}}$ to a rotation matrix $\boldsymbol{R}_{\mathrm{D}}^{\mathrm{E}}$, we obtain:

$$\boldsymbol{R}_{\mathrm{D}}^{\mathrm{E}} = \begin{bmatrix} 1 - 2q_y^2 - 2q_z^2 & 2q_xq_y - 2q_zq_w & 2q_xq_z + 2q_yq_w \\ 2q_xq_y + 2q_zq_w & 1 - 2q_x^2 - 2q_z^2 & 2q_yq_z - 2q_xq_w \\ 2q_xq_z - 2q_yq_w & 2q_yq_z + 2q_xq_w & 1 - 2q_x^2 - 2q_y^2 \end{bmatrix}. \quad (26)$$

The rotation matrix from ECS to 3-D MCS, $\boldsymbol{R}_{\mathrm{E}}$, is constant, and the rotation matrix from DCS to 3-D MCS is given by:

$$\boldsymbol{R}_{\mathrm{D}} = \boldsymbol{R}_{\mathrm{E}} \cdot \boldsymbol{R}_{\mathrm{D}}^{\mathrm{E}}. \quad (27)$$

After defining these coordinate systems, it is essential to accurately detect the step events, and calculate the step lengths and yaws in the PDR system. The step detection relies on the smartphone acceleration $\boldsymbol{a}$ in 3-D MCS, but the linear acceleration $\boldsymbol{a}^{\mathrm{D}}$ obtained from the accelerometer is in DCS. We calculate the acceleration $\boldsymbol{a}$ by:

$$\boldsymbol{a} = \boldsymbol{R}_{\mathrm{D}} \cdot \boldsymbol{a}^{\mathrm{D}}. \quad (28)$$

Let the current time be k, and the sequence of the vertical component of $\boldsymbol{a}$ be $\{z_i\}_{i=1}^{k}$. The proposed conditions for determining the step event are as follows:

$$\begin{cases} z_{k-h} = \max\limits_{i=k-2h}^{k} z_i, & (29a) \\ z_{k-h} > z_{\mathrm{th}}, & (29b) \\ k - h - h' > k_{\mathrm{th}}, & (29c) \end{cases}$$

where h is half of the window size; z_{th} is the threshold for maximum step acceleration; k_{th} is the threshold for minimum step interval; and h' is the last step event time. Only when these three conditions are simultaneously satisfied can time $k - h$ be recognized as a step event. At this time, the peak-to-peak value of the acceleration within this $2h$ window is calculated as:

$$z_{\mathrm{pp}} = z_{k-h} - \min_{i=k-2h}^{k} z_i, \quad (30)$$

and the step length s is estimated as [44]:

$$s = \beta \sqrt[4]{z_{\mathrm{pp}}}. \quad (31)$$

The step direction vector in 3-D MCS is estimated as:

$$\boldsymbol{d}'_k = \begin{cases} \boldsymbol{R}_{\mathrm{D}}[0, 1, 0]^{\mathsf{T}}, & k \le k_0, \\ \boldsymbol{R}_{\mathrm{M}}(\boldsymbol{\omega}^{\mathrm{D}}, \boldsymbol{a}_g^{\mathrm{D}}, \boldsymbol{m}^{\mathrm{D}}; \theta_{k_0}) \boldsymbol{R}_{\mathrm{D}}[0, 1, 0]^{\mathsf{T}}, & k > k_0, \end{cases} \quad (32)$$

where $\boldsymbol{R}_{\mathrm{M}}(\ \cdot\ ; \theta_{k_0})$ represents the orientation filter proposed by Madgwick *et al.* [45] with initial yaw θ_{k_0}. This filtering algorithm takes the angular acceleration $\boldsymbol{\omega}^{\mathrm{D}}$, acceleration $\boldsymbol{a}_g^{\mathrm{D}}$ that includes gravity, and magnetic flux density $\boldsymbol{m}^{\mathrm{D}}$ as inputs. The yaw at time k is then estimated as:

$$\theta_k = \mathrm{atan2}(\boldsymbol{d}_k), \quad (33)$$

where $\boldsymbol{d}_k$ is the normalized projection of $\boldsymbol{d}'_k$ from 3-D MCS to 2-D MCS. In this way, we obtain the step length s_k and yaw θ_k if a step event is detected at time k.

C. Fusion with PF

We use the PF to fuse the BLE result in Section III and the PDR result in Section IV-B. A PF at time k can be defined as $\mathcal{P}^{(k)} = \{\boldsymbol{x}_i^{(k)}, w_i^{(k)}\}_{i=1}^{m}$, where $\boldsymbol{x}_i^{(k)}$ is the position of i-th particle, and $w_i^{(k)}$ is its weight. When $k = 0$, we set the initial state as $\boldsymbol{x}_i^{(0)} = \overline{\boldsymbol{x}}_B^{(0)}$, $w_i^{(0)} = 1/m$, where $\overline{\boldsymbol{x}}_B^{(0)}$ is the average of BLE positioning results during initialization.

Function 1: *Raycast*

Input: Map: $\boldsymbol{M}(\boldsymbol{x})$; Start point: $\boldsymbol{x}_1$; End point: $\boldsymbol{x}_2$; [Update step: $\delta = 0.05$];
Output: Hit flag: `hit`; Hit point: $\boldsymbol{h}$;

```
hit = False;
if x_1 − x_2 = 0 then
    return hit = (M(x_1) > 0), h = hit ? x_1 : Null;
N = Round(‖x_2 − x_1‖/δ);
x_n = (x_2 − x_1)/‖x_2 − x_1‖;
for k = 0 : N do
    if M(x_1 + kδx_n) > 0 then
        return hit = True, h = x_1 + kδx_n;
if ! hit then return hit = False, h = Null;
```

The state transition of the i-th particle can be modeled as:

$$\widehat{\boldsymbol{x}}_i^{(k)} = \boldsymbol{x}_i^{(k-1)} + (s_{k-1} + \nu_{s,i}) \cdot \begin{bmatrix} \cos(\theta_{k-1} + \nu_{\theta,i}) \\ \sin(\theta_{k-1} + \nu_{\theta,i}) \end{bmatrix}, \quad (34)$$

where $\nu_{s,i}$ and $\nu_{\theta,i}$ are the zero-mean PDR noise, and are modeled as the uniform distribution. In the PF, we use the Monte Carlo method to approximate (5) and (8) by:

$$\begin{cases} p(\boldsymbol{x}^{(k)}|\mathcal{Z}^{(k)}) \approx \sum_{i=1}^{m} \widetilde{w}_i^{(k)} \delta(\boldsymbol{x}^{(k)} - \widehat{\boldsymbol{x}}_i^{(k)}), & (35a) \\ \widehat{\boldsymbol{x}} \approx \sum_{i=1}^{m} \widetilde{w}_i^{(k)} \widehat{\boldsymbol{x}}_i^{(k)}, & (35b) \end{cases}$$

where $\delta(\cdot)$ is the Dirac function. According to (5), the normalized particle weights $\{\widetilde{w}_i^{(k)}\}_{i=1}^m$ should be calculated as normalized $p(\boldsymbol{x}_B^{(k)}|\boldsymbol{x}_i^{(k)})$. Therefore, based on the assumption of Gaussian noise [39], these weights are calculated by:

$$w_i^{(k)} = \frac{1}{\sqrt{2\pi\sigma_x^2}} \exp\left[-\frac{\|\boldsymbol{x}_B^{(k)} - \widehat{\boldsymbol{x}}_i^{(k)}\|^2}{2\sigma_x^2}\right], \quad (36)$$

and then be normalized. Finally, by resampling the PF [46], the estimated position $\widehat{\boldsymbol{x}}$ is calculated as the average of all particles. As mentioned before, $\widehat{\boldsymbol{x}}$ is a numerical approximation of (8) and does not take constraint (4) into account. We will address this problem in the following subsection.

D. Floor Plan Assisted Post Processing

To integrate floor plan constraint (4) into our system, we propose the PPC algorithm, which consists of two parts: *Correction Determination* and *Position Correction*. The former is responsible for deciding whether the initial estimation $\widehat{\boldsymbol{x}}$ in Section IV-C needs correction, and the latter applies specific corrections to the estimated position based on different determination conditions.

1) Correction Determination: We first define the *Raycast* function, which is summarized in **Function 1**. In *Raycast*, we move from a start point incrementally towards the end point, until it is reached. If an obstacle is encountered during this process, the *Raycast* returns **True** and the first contact point $\boldsymbol{h}$ (also referred to as the *hit point*). *Raycast* efficiently detects whether there is an obstacle between two points; if an obstacle exists, it can find the hit point with a time complexity of $\mathcal{O}(n)$.

At a time k, perform *Raycast* from the previous position $\boldsymbol{x}^{(k-1)}$, to the estimated position $\widehat{\boldsymbol{x}}$. If the hit point $\boldsymbol{h}$ is obtained, it is considered that moving from $\boldsymbol{x}^{(k-1)}$ to $\widehat{\boldsymbol{x}}$ is not feasible. The infeasible step necessitates a position correction, which typically includes step length correction and yaw correction. Then, a candidate rotation angle sequence $\boldsymbol{\Phi} = \{\pm i\phi\}_{i=1}^N$ is defined. In this sequence, ϕ is a unit rotation angle, and the elements in $\boldsymbol{\Phi}$ are arranged in ascending order of their absolute values.

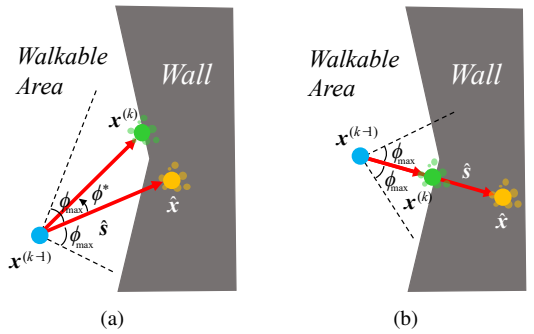

Fig. 5: Position correction part I: yaw correction is needed. In (a), the step is rotated by an optimal angle ϕ^* towards the *Walkable* area (Case 1); while in (b), the step is considered blocked (Case 2).

From Section IV-A3, we can determine the map feature $\boldsymbol{M}(\boldsymbol{h})$ of the hit point $\boldsymbol{h}$:

(i) If $\boldsymbol{h}$ is *Wall*, i.e., $\boldsymbol{M}(\boldsymbol{h}) = 1$, it is assumed to correct yaw by searching both sides for *Walkable* areas, i.e., to find the best angle by directly rotating in the order of $\boldsymbol{\Phi}$.

(ii) If $\boldsymbol{h}$ is *Door*, i.e., $\boldsymbol{M}(\boldsymbol{h}) = 0.5$, it is necessary to determine whether the user should pass through the *Door*, since *Doors* are defined as conditionally passable obstacles. If it is determined that the user should not pass through the *Door*, the PPC algorithm assumes that the yaw should be corrected towards the inside of the *Room*.

We use the incident angle α of the estimated step vector $\widehat{\boldsymbol{s}}$ to determine whether the user passes through the *Door*. Let $\widehat{\boldsymbol{s}} = \widehat{\boldsymbol{x}} - \boldsymbol{x}^{(k-1)}$, and the incident angle α of $\widehat{\boldsymbol{s}}$ to the obstacle can then be calculated as:

$$\alpha = \langle \boldsymbol{n}_h, -\widehat{\boldsymbol{s}} \rangle, \quad (37)$$

where $\boldsymbol{n}_h$ is the normal vector at $\boldsymbol{h}$, obtained by transforming the image gradient vector $\nabla \boldsymbol{I}(\boldsymbol{h}^{\mathrm{I}})$ from ICS to MCS; $\langle \boldsymbol{x}, \boldsymbol{y} \rangle$ is the included angle formed by vectors $\boldsymbol{x}$ and $\boldsymbol{y}$. When α is larger than a threshold α_0, it is assumed that the user should not pass through the *Door*, and in this case, we rotate the estimated step $\widehat{\boldsymbol{s}}$ by a positive and a negative angle, ϕ_+ and ϕ_-, respectively. Then the resulting incident angles, α_+ and α_-, are compared. According to the geometric principle, rotating towards the inside of *Room* is equivalent to rotating in the direction of increasing incident angles. This allows the determination of the sign of the correction angle, i.e., the direction of rotation, and $\boldsymbol{\Phi}$ is filtered to retain only the elements corresponding to the determined sign, while maintaining their original order.

2) Position Correction: In Section IV-D1, we proposed the method for determining whether the yaw should be corrected, and it was concluded that in PPC algorithm, the only case where yaw correction is not required is when the pedestrian

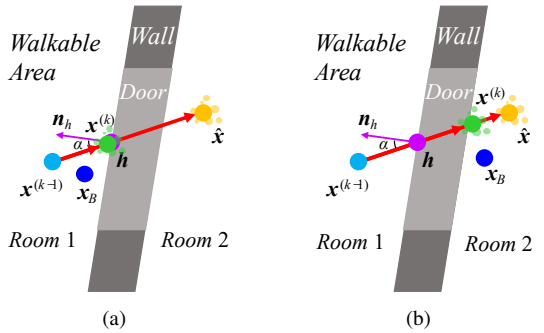

Fig. 6: Position correction part II: yaw correction is unnecessary. In (a), the step is considered blocked by the *Door* (Case 2); while in (b), the pedestrian is considered to pass through the *Door* (Case 3).

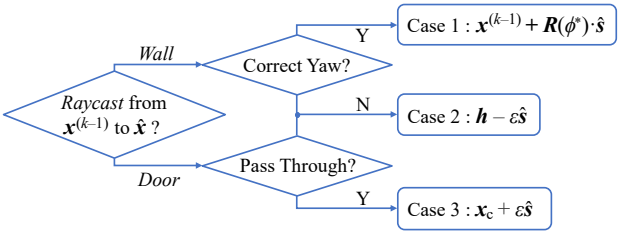

Fig. 7: Flow chart of position correction in PPC algorithm.

passes through a *Door*.

(i) If the yaw correction is needed, as shown in Fig. 5(a), we find the optimal correction rotation angle by sequentially traversing all candidate angles in $\boldsymbol{\Phi}$ and then determining the optimal corrected position. $\forall \phi' \in \boldsymbol{\Phi}$, we can construct a rotation matrix by:

$$\boldsymbol{R}(\phi') \triangleq \begin{bmatrix} \cos\phi' & -\sin\phi' \\ \sin\phi' & \cos\phi' \end{bmatrix}, \tag{38}$$

and rotate $\widehat{\boldsymbol{s}}$ to obtain a test point $\boldsymbol{x}_{\mathrm{t}}(\phi')$:

$$\boldsymbol{x}_{\mathrm{t}}(\phi') = \boldsymbol{x}^{(k-1)} + \boldsymbol{R}(\phi') \cdot f\widehat{\boldsymbol{s}}, \tag{39}$$

where $f \geq 1$ is a scale factor. Next, we follow the order of $\boldsymbol{\Phi}$, sequentially searching for the optimal rotation angle ϕ^* with the smallest absolute value, such that *Raycast* from $\boldsymbol{x}^{(k-1)}$ to $\boldsymbol{x}_{\mathrm{t}}(\phi')$ returns **False**, which indicates that this path is feasible without any obstruction:

$$\phi^* = \arg\min_{\phi' \in \boldsymbol{\Phi}} |\phi'| \tag{40}$$

$$\text{s.t.} \quad \mathrm{Raycast}(\boldsymbol{M}, \boldsymbol{x}^{(k-1)}, \boldsymbol{x}_{\mathrm{t}}(\phi')) = \textbf{False}. \tag{40a}$$

Then, the corrected position defined as:

$$\boldsymbol{x}^{(k)} = \boldsymbol{x}^{(k-1)} + \boldsymbol{R}(\phi^*) \cdot \widehat{\boldsymbol{s}}. \tag{41}$$

If a suitable rotation angle cannot be found within sequence $\boldsymbol{\Phi}$, i.e., $\forall \phi' \in \boldsymbol{\Phi}$, $\mathrm{Raycast}(\boldsymbol{M}, \boldsymbol{x}^{(k-1)}, \boldsymbol{x}_{\mathrm{t}}(\phi')) = \textbf{True}$, we can only assume that the step is blocked by an obstacle. As shown in Fig. 5(b), in this case, a step length correction is applied instead, by moving a small distance backward from the hit point $\boldsymbol{h}$ to *Walkable* area, yielding the corrected position:

$$\boldsymbol{x}^{(k)} = \boldsymbol{h} - \varepsilon\widehat{\boldsymbol{s}}. \tag{42}$$

Algorithm 2: PPC Algorithm

Input: Previous position: $\boldsymbol{x}^{(k-1)}$; Estimated step: $\widehat{\boldsymbol{s}}$;
Map: $\boldsymbol{M}(\boldsymbol{x})$; Estimated particles: $\{\widehat{\boldsymbol{x}}_i^{(k)}\}_{i=1}^m$;
Output: Estimated position: $\boldsymbol{x}^{(k)}$; Particles: $\mathcal{P}^{(k)}$;

Set candidate angles as $\boldsymbol{\Phi} = [\pm j\phi$ **for** $j = 1, 2, \ldots, N]$;
Obtain flag `hit` and point $\boldsymbol{h}$ by $\mathrm{Raycast}(\boldsymbol{M}, \boldsymbol{x}^{(k-1)}, \widehat{\boldsymbol{x}})$;
if `hit` ***and*** $\boldsymbol{h} \neq \boldsymbol{x}^{(k-1)}$ **then**
  if $\boldsymbol{h}$ *is* ***Door*** **then**
    Obtain $\boldsymbol{h}^{\mathrm{I}}$ by transforming $\boldsymbol{h}$ into ICS;
    Calculate the image gradient vector $\nabla \boldsymbol{I}(\boldsymbol{h}^{\mathrm{I}})$;
    Obtain $\boldsymbol{n}_h$ by transforming $\nabla \boldsymbol{I}(\boldsymbol{h}^{\mathrm{I}})$ into MCS;
    Obtain the incident angle α by (37);
    if $\alpha > \alpha_0$ **then**
      $\alpha_+ = \langle \boldsymbol{n}_h, -\boldsymbol{R}(\phi_+) \cdot \widehat{\boldsymbol{s}} \rangle$;
      $\alpha_- = \langle \boldsymbol{n}_h, -\boldsymbol{R}(\phi_-) \cdot \widehat{\boldsymbol{s}} \rangle$;
      $\boldsymbol{\Phi} = (\alpha_+ > \alpha_-)$ **?** $\boldsymbol{\Phi}[\boldsymbol{\Phi} > 0]$ **:** $\boldsymbol{\Phi}[\boldsymbol{\Phi} < 0]$;
    `correct_yaw` $= (\alpha > \alpha_0)$;
  else
    `correct_yaw` $=$ **True**;
  if `correct_yaw` **then**
    Find the optimal rotation angle $\phi^* \in \boldsymbol{\Phi}$ by (40);
    if ϕ^* *is found* **then**
      Case 1: Correct the position $\boldsymbol{x}^{(k)}$ by (41);
    else
      Case 2: Correct the position $\boldsymbol{x}^{(k)}$ by (42);
  else
    Check the *Room* in which $\boldsymbol{x}_B$ is;
    Case 2/3: Correct the position $\boldsymbol{x}^{(k)}$ by (43);
  Update the particles by (44);

(ii) If the yaw correction is unnecessary, even though the incident angle suggests that the user should pass through the *Door*, it is essential to first determine whether the user's current *Room* has changed, since passing through a *Door* always implies a *Room* change. If the *Room* remains unchanged, the user should not be permitted to pass through the *Door*.

Since all the internal contours of the map are obtained in the offline phase in Section IV-A2, it is easy to determine the *Room* of the last result $\boldsymbol{x}^{(k-1)}$, i.e. the contour that contains $\boldsymbol{x}^{(k-1)}$. Since the estimated results of GML algorithm are typically accurate enough to distinguish different *Rooms*, we use $\boldsymbol{x}_B$ as the basis for determining the current *Room*. As shown in Fig. 6(a), if $\boldsymbol{x}_B$ is still in the previous *Room*, we still consider it to be blocked by the *Door*, and thus, the result is corrected by moving from the hit point backward to the *Walkable* area. Otherwise, in Fig. 6(b), we consider the user to pass through the *Door* in this step. We identify the closest point $\boldsymbol{x}_{\mathrm{c}}$ from all the contours, and correct the result by moving a small step forward from $\boldsymbol{x}_{\mathrm{c}}$ into *Walkable* area, completing the action of passing through the *Door*:

$$\boldsymbol{x}^{(k)} = \begin{cases} \boldsymbol{h} - \varepsilon\widehat{\boldsymbol{s}}, & \textit{if } \boldsymbol{x}_B \textit{ is in previous Room}, \\ \boldsymbol{x}_{\mathrm{c}} + \varepsilon\widehat{\boldsymbol{s}}, & \textit{otherwise}. \end{cases} \tag{43}$$

Finally, if post-processing correction is applied to $\widehat{\boldsymbol{x}}$, the particles in the PF also need to be corrected accordingly:

$$\boldsymbol{x}_i^{(k)} = \widehat{\boldsymbol{x}}_i^{(k)} + \boldsymbol{x}^{(k)} - \widehat{\boldsymbol{x}}. \tag{44}$$

TABLE I
KEY EXPERIMENTAL PARAMETERS

Device Parameter		Value	Algorithm Parameter		Value
BLE Beacon	Model	RF-star RF-B-SR1	FP-BP	Floor plan resolution	$r = 1/0.07$ m^{-1}
	Broadcast interval	200 ms		Virtual grid interval	$I_M = 0.3$ m
	Transmission power	0 dBm		BLE estimation interval	250 ms
	Advertising mode	iBeacon		BLE Kalman filter	$q_K = 0.16$, $r_K = 16$
Smartphone	Model	HONOR Magic 6		PF particle number	$m = 500$
	Mobile processor	Snapdragon 8 Gen3		PF particle noise	$\lvert\nu_s\rvert \leq 0.05$ m, $\lvert\nu_\theta\rvert \leq 10^\circ$
	Operating system	Android 15		PF fusion variance	$\sigma_x^2 = 0.1$
	BLE scan mode	Low latency		PPC candidate angles	$\mathbf{\Phi} = \{\pm i \cdot 5^\circ\}_{i=1}^{12}$
	IMU sample rate	60 Hz		PPC test scale factor	$f = 1.5$

(a) (b)

Fig. 8: a) BLE beacons in the experimental area; b) FP-BP prototype on the smartphone.

If no post processing is performed, the output of the algorithm is simply $\boldsymbol{x}^{(k)} = \widehat{\boldsymbol{x}}$.

To summarize the *Position Correction* part in PPC algorithm, we divide the position correction into three cases. (i) In Case 1, we find the optimal correction rotation angle and implement yaw correction; (ii) In Case 2, we treat this case as being blocked by an obstacle and implement step length correction; (iii) In Case 3, we assume the user has passed through the *Door* and perform a *Room* switch. The position correction process of PPC algorithm is illustrated in Fig. 7.

The PPC algorithm is summarized in **Algorithm 2**. Besides, it is worth noting that the number of consecutive occurrences of Case 2 should be counted. When Case 2 occurs multiple times consecutively, it indicates that the user has been blocked by an obstacle repeatedly. Since such a situation is unlikely to occur during normal walking, it is considered that the positioning result has deviated significantly and is therefore unreliable. In this case, the estimated result $\boldsymbol{x}^{(k)}$ should be corrected to $\boldsymbol{x}_B$ to avoid excessive errors.

V. EXPERIMENTAL SETUP AND RESULTS

In this section, a prototype is established to implement FP-BP, and experiments are conducted to verify its performance and feasibility. Fig. 8 shows the experimental area and prototype of FP-BP, and key experimental parameters are listed in Table I. Next, we will detail the implementation of the experiments and analyze the results.

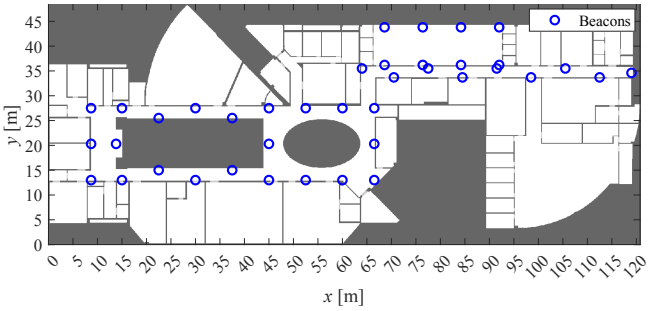

Fig. 9: Beacon deployment in the experimental area.

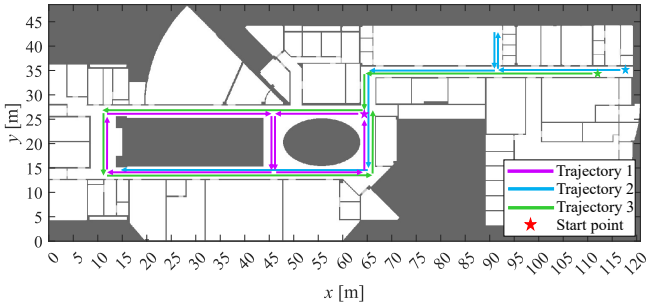

Fig. 10: A brief diagram of the experimental trajectories.

A. Experimental Setup

The experimental area is located in a building with a ceiling height of approximately 2.5 m, and a total area of about 5760 m^2. In our experiments, a total of 39 beacons are deployed on the ceiling of this floor. These beacons, as shown in Fig. 8(a), have distinct UUIDs and are deployed at the coordinates shown in Fig. 9.

In the experiments, we set the tester to walk along a specific trajectory at a speed of approximately 1.0 m/s, holding the smartphone facing forward (i.e., the y^{D}-axis of the phone is directed forward), with the step length fixed at 0.6 m. To verify the robustness of FP-BP, we set up three trajectories, as shown in Fig. 10. The total lengths of these trajectories are 316.8 m, 137.4 m and 187.8 m, respectively. In particular, for trajectory 1, the tester walks two laps for one trial; for trajectory 2, there are two *Room* switch events, whereas other trajectories have none. Among them, trajectory 1 is considered the most representative, and thus Sections V-B and V-C present the results of 10 trials of trajectory 1 conducted by two testers.

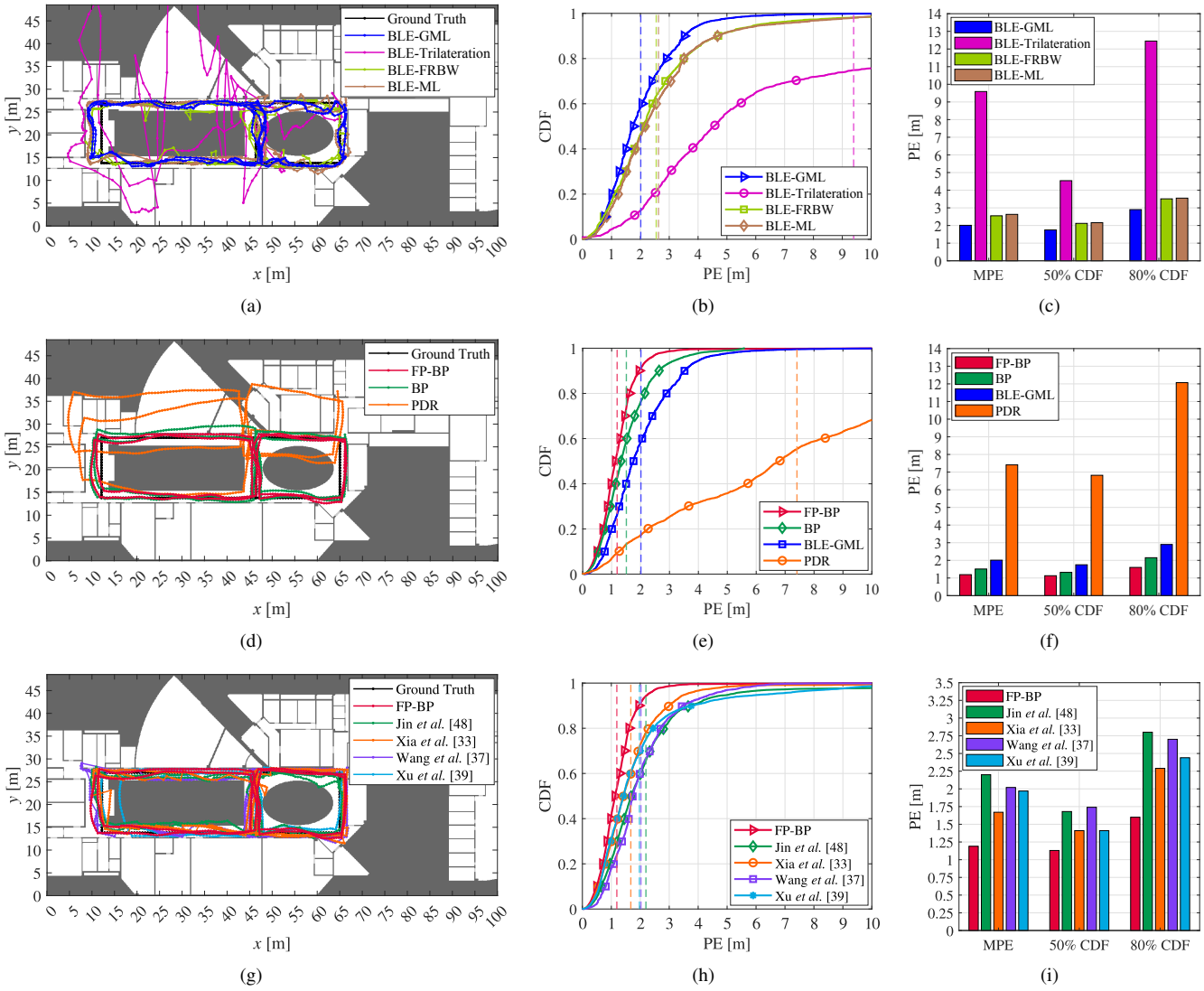

Fig. 11: Experimental results of trajectory 1. (a)–(c): Comparison of GML with BLE baseline algorithms. (d)–(f): Comparison of FP-BP in different cases. (g)–(i): Comparison of FP-BP with baseline algorithms.

The comparisons across these three trajectories are presented in Section V-D.

To evaluate the positioning performance, we use the following metrics: (i) The 2-D position error (PE), which is defined as the distance between the estimated position and the ground truth in MCS. (ii) The average of multiple PEs, termed MPE. (iii) The average of multiple computation times, termed MCT.

B. BLE Positioning Results

We first analyze the experimental results of the proposed GML algorithm. In terms of baselines, in addition to the traditional maximum likelihood (ML) algorithm in our previous work [1], we also conduct another two common algorithms: the linear least squares (LLS)-based trilateration [23] and the filtered RSSI and beacon weight (FRBW) algorithm [47]. Note that: (i) The LLS-based trilateration takes all beacons into calculation. (ii) For the FRBW algorithm, the weight adjustable degree g is set to 5, and only the top 3 beacons with the largest RSSIs are involved in the calculation. (iii) We apply the same mean filtering used in GML algorithm to the results of all algorithms. Taking the step moments detected by FP-BP as the reference, we record the BLE estimated position at each step moment, and calculate its PE relative to the ground truth position.

The experimental results are shown in Fig. 11(a). It can be observed that despite using KF and mean filtering, the positioning results estimated by the trilateration still exhibit significant fluctuations, with some results deviating considerably from the ground truth. Both GML and FRBW algorithms successfully constrained their results within the experimental area. However, FRBW algorithm still has some estimated positions appearing inside obstacles, which is avoided by the proposed GML algorithm.

Figs. 11(b) and (c) present the comparison of performance metrics between GML and baselines. It can be seen that GML algorithm achieves an MPE of 2.01 m, which is the lowest among all baselines, while the MPEs of trilateration,

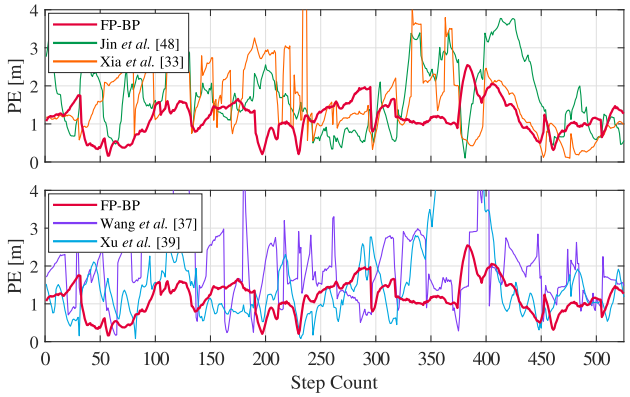

Fig. 12: PE versus step count for FP-BP and baseline algorithms.

FRBW, and ML algorithms are 9.39 m, 2.55 m, and 2.63 m, respectively. Moreover, in terms of 80% CDF corresponding PE, the GML algorithm results in 2.90 m, whereas FRBW and ML result in 3.51 m and 3.55 m, respectively. These demonstrate that the GML algorithm significantly outperforms these baselines in terms of positioning performance.

C. FP-BP Positioning Results

To assess the performance of FP-BP, we conduct the fusion positioning systems proposed by Jin *et al.* [48], Xia *et al.* [33], Wang *et al.* [37] and Xu *et al.* [39] as baselines for comparison. In particular: (i) The system proposed by Jin *et al.* [48] is a common BLE/PDR fusion system without floor plan integration. (ii) Xia *et al.* [33] introduce the floor plan into the traditional PF-based BLE/PDR fusion system. In their system, the weights of particles within obstacle areas are reset to zero. (iii) Wang *et al.* [37] identify landmarks such as access points, doors, corners, and walls in the floor plan, and implement specify position calibrations in their system. Note that due to the complexity of this floor plan, it is challenging to define the direction of corners. Therefore, only the positions of the corners are matched in our experiments. (iv) Xu *et al.* [39] proposed an optimization scheme for particle re-initialization based on [33], taking into account the problem of particle depletion and result divergence. Note that we utilize the KF-processed BLE RSSIs in place of the WiFi fine timing measurement (FTM) due to the challenges in implementing time-based BLE positioning [13].

The experimental results are shown in Figs. 11(d)–(i), and 12. Fig. 11(d) demonstrates the experimental results of FP-BP in different cases, including FP-BP, FP-BP without the PPC algorithm (denoted as BP), and PDR. It is evident that although the initial position of PDR is set as the ground truth, the PE of PDR gradually increases as sensor errors accumulate, eventually deviating significantly from the ground truth. After fusing the BLE estimated position using PF, the cumulative error of BP is significantly reduced; however, many positioning results still "pass through walls" and appear outside the intended walkable area. Finally, by applying the PPC algorithm to incorporate the floor plan, the FP-BP algorithm successfully confines these positioning points within the correct area.

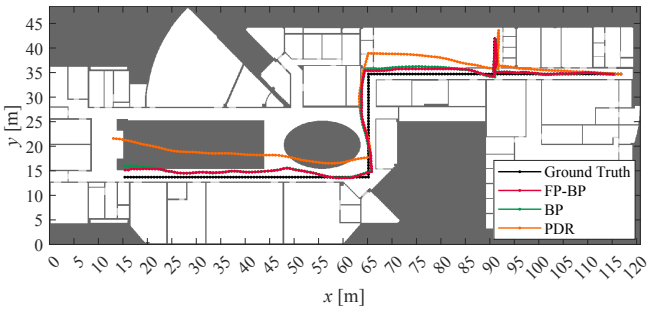

(a) Results of trajectory 2.

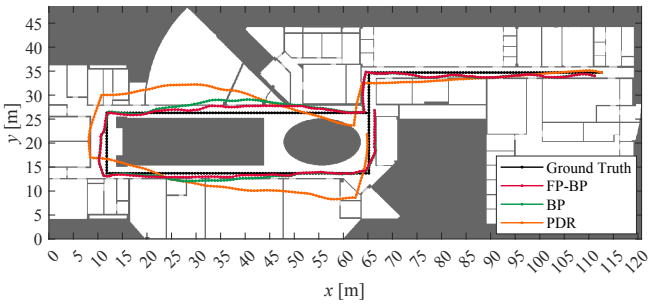

(b) Results of trajectory 3.

Fig. 13: Experimental results of FP-BP across trajectories.

Figs. 11(e) and (f) show the comparison of PE for FP-BP in different cases, including the proposed GML algorithm. In these cases, we can see FP-BP achieves the lowest MPE of 1.19 m, followed by BP with an MPE of 1.51 m. The system that uses PDR solely has the largest MPE of 7.41 m, indicating that the cumulative errors of IMU significantly increase as the user walks further. However, after incorporating BLE, the MPE drops noticeably, reaching below 2 m, demonstrating that BLE positioning effectively helps mitigate the cumulative error. Additionally, after integrating PDR, BP outperforms GML in terms of accuracy, suggesting that PDR provides valuable movement information that enhances BLE positioning. Finally, we observe that after applying the PPC algorithm, the MPE of FP-BP is further reduced by approximately 0.3 m, which clearly demonstrates that floor plan integration significantly improves the positioning accuracy by 20%. Additionally, for FP-BP, the 50% and 80% CDF corresponding PEs are 1.13 m and 1.60 m, respectively, representing improvements of 17% and 26% compared to BP. Overall, FP-BP achieves the best performance among all these cases.

To further evaluate the performance of FP-BP, in Figs. 11(g)–(i) and 12, we take the baseline systems [33], [37], [39], [48] for comparison. In Fig. 11(g), we can see that due to the lack of floor plan integration, some estimated positions of [48] appear inside obstacles. Additionally, despite the incorporation of the floor plan, baseline [39] still cannot prevent some results from erroneously appearing within obstacles. Other algorithms, including FP-BP, have successfully avoided this "wall-crossing" problem.

Fig. 11(h) shows the CDFs of PE for FP-BP and baselines. We can observe that among these algorithms, FP-BP achieves the lowest MPE at 1.19 m, consistent with Fig. 11(e). In

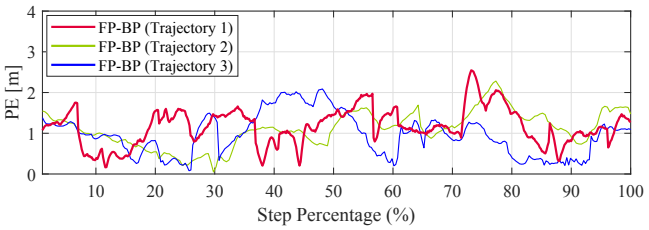

Fig. 14: PE versus step percentage for FP-BP across trajectories.

TABLE II
EXPERIMENTAL RESULTS OF FP-BP

Trajectory		MPE [m]		50%CDF [m]		80%CDF [m]		MCT [ms]	
No.	Steps	FP-BP	BP	FP-BP	BP	FP-BP	BP	*GML*	*Fusion*
1	528	**1.19**	1.51	**1.13**	1.32	**1.60**	2.14	5.57	4.67
2	229	**1.08**	1.25	**1.01**	1.22	**1.48**	1.56	4.88	5.35
3	313	**0.89**	1.18	**0.80**	1.07	**1.33**	1.58	5.23	4.58

contrast, the MPEs of the baselines are 2.20 m [48], 1.67 m [33], 2.02 m [37], and 1.97 m [39], respectively, which are significantly larger that of FP-BP, and FP-BP improves positioning accuracy by over 28% compared with these baselines. In Fig. 11(i), we can further observe that in terms of 80% CDF corresponding PE, the FP-BP algorithm results in 1.60 m, while the PEs of these baselines are all over 2 m.

Fig. 12 demonstrates the PEs for FP-BP and baseline algorithms as the step count increases in a single experiment. It is evident that all these algorithms effectively reduce cumulative errors, as their PEs do not significantly increase with the step count. However, the results of [33], [37], [39], [48] exhibit significant fluctuations, with peak PEs exceeding 3 m, indicating that these algorithms struggle to provide accurate and stable positioning in certain areas. In contrast, the PE of FP-BP remains more stable, with about 90% of PEs kept within 2 m, and no instances exceeding 3 m. These results indicate that FP-BP demonstrates superior performance compared to existing fusion-based positioning systems.

D. Results Comparison Across Trajectories

To verify the robustness of FP-BP under various trajectories, we further conduct experiments to compare the results of FP-BP across three trajectories, as shown in Figs. 13, 14 and Table II. In Fig. 13, we can see that similar to Fig. 11(d), FP-BP effectively constrains the positioning results within the correct *Room*. Moreover, when the user passes through a *Door* into another *Room*, it accurately handles this *Room* switch event.

In Fig. 14, we can observe that across the three trajectories, as the step count increases, FP-BP similarly effectively mitigates cumulative errors, keeping almost all the PEs within 2 m. Additionally, Table II indicates that FP-BP demonstrates excellent positioning performance across these three trajectories, achieving MPEs of 1.08 m and 0.89 m for trajectories 2 and 3, respectively. In contrast, the BP system without floor plan integration reaches MPEs of 1.25 m and 1.18 m for the same trajectories. Furthermore, the 50% and 80% CDF corresponding PEs of FP-BP are also less than those of BP. These results indicate that FP-BP operates stably in indoor environments, remaining unaffected by changes in trajectory, and exhibits both high accuracy and strong robustness.

Finally, we analyze the computational delay of FP-BP to evaluate the system's complexity. On the Android platform (see Table I for smartphone parameters), the *GML* and *Fusion* modules are implemented as independent `Runnable` tasks respectively, and each of them is executed at a fixed interval. Therefore, we separately report the MCT of these modules within FP-BP. From Table II, it can be seen that both these modules keep the MCT within 6 ms for all three trajectories, which are far less than the BLE signal broadcasting interval and position estimation interval. This clearly demonstrates that the FP-BP system has strong real-time performance, low latency, and maintains good robustness through various experiments.

VI. CONCLUSION

In this paper, we have proposed the FP-BP algorithm, which can fully utilize the floor plan information to achieve real-time and accurate indoor positioning, without any limitations on indoor layout or map geometry. We have also proposed the GML algorithm to enhance RSSI-based BLE positioning. In particular, based on the accurate extraction of map features, a floor plan preprocessing method is first performed in the offline phase to construct an indoor map. In the online phase, based on an MLE model, we apply the GML algorithm to obtain the BLE result. Then, smartphone sensor data is fused by a PF to perform an initial estimation. Finally, based on the preprocessed indoor map, floor plan prior information is integrated through the proposed PPC algorithm by applying specific post-correction to the initial estimation. To verify the performance of FP-BP, we have conducted experiments in the public area with a total area of over 5,000 m^2 in a building, and the results indicate that the FP-BP algorithm can achieve a mean positioning accuracy of 1.19 m, outperforming other floor plan-fused baselines by over 28%. Moreover, FP-BP algorithm has also demonstrated superior real-time performance on mobile devices. Therefore, it holds great promise for positioning in large-scale indoor scenarios.

REFERENCES

[1] W. Pan, Y. Yang, Z. Zhu, and B. Zhang, "Floor-plan-assisted fusion positioning using Bluetooth and pedestrian dead reckoning," in *IEEE Int. Conf. Commun. Workshops (ICC Workshops)*, Montreal, Canada, Jun. 2025, pp. 1–6.

[2] Y. Yang *et al.*, "Positioning using wireless networks: Applications, recent progress, and future challenges," *IEEE J. Sel. Areas Commun.*, vol. 42, no. 9, pp. 2149–2178, Sept. 2024.

[3] J. C. J. Koelemeij, H. Dun, C. E. V. Diouf, E. F. Dierikx, G. J. M. Janssen, and C. C. J. M. Tiberius, "A hybrid optical–wireless network for decimetre-level terrestrial positioning," *Nature*, vol. 611, pp. 473–478, Nov. 2022.

[4] Y. Dong, T. Arslan, and Y. Yang, "An encoded LSTM network model for WiFi-based indoor positioning," in *IEEE 12th Int. Conf. Indoor Position. Indoor Navig. (IPIN)*, Beijing, China, Sept. 2022, pp. 1–6.

[5] C. K. M. Lee, C. M. Ip, T. Park, and S. Chung, "A Bluetooth location-based indoor positioning system for asset tracking in warehouse," in *IEEE Int. Conf. Ind. Eng. Eng. Manage. (IEEM)*, Macao, China, Dec. 2019, pp. 1408–1412.

[6] J. Zhang *et al.*, "Robust RFID based 6-DoF localization for unmanned aerial vehicles," *IEEE Access*, vol. 7, pp. 77 348–77 361, 2019.

[7] Z. Zhu, Y. Yang, M. Chen, C. Guo, J. Hao, and S. Cui, "Visible light positioning with visual odometry: A single luminaire based positioning algorithm," *IEEE Trans. Commun.*, vol. 72, no. 8, pp. 4978–4991, Aug. 2024.

[8] Y. Zhang, X. Tan, and C. Zhao, "UWB/INS integrated pedestrian positioning for robust indoor environments," *IEEE Sensors J.*, vol. 20, no. 23, pp. 14 401–14 409, Dec. 2020.

[9] K. E. Jeon, J. She, P. Soonsawad, and P. C. Ng, "BLE beacons for internet of things applications: Survey, challenges, and opportunities," *IEEE Internet Things J.*, vol. 5, no. 2, pp. 811–828, Apr. 2018.

[10] P. Spachos and K. N. Plataniotis, "BLE beacons for indoor positioning at an interactive IoT-based smart museum," *IEEE Syst. J.*, vol. 14, no. 3, pp. 3483–3493, Feb. 2020.

[11] P. C. Ng, P. Spachos, J. She, and K. N. Plataniotis, "A kernel method to nonlinear location estimation with RSS-based fingerprint," *IEEE Trans. Mob. Comput.*, vol. 22, no. 8, pp. 4388–4404, Aug. 2023.

[12] R. Faragher and R. Harle, "Location fingerprinting with Bluetooth low energy beacons," *IEEE J. Sel. Areas Commun.*, vol. 33, no. 11, pp. 2418–2428, Nov. 2015.

[13] Y. Zhuang, C. Zhang, J. Huai, Y. Li, L. Chen, and R. Chen, "Bluetooth localization technology: Principles, applications, and future trends," *IEEE Internet Things J.*, vol. 9, no. 23, pp. 23 506–23 524, Dec. 2022.

[14] P. S. Farahsari, A. Farahzadi, J. Rezazadeh, and A. Bagheri, "A survey on indoor positioning systems for IoT-based applications," *IEEE Internet Things J.*, vol. 9, no. 10, pp. 7680–7699, May 2022.

[15] Bluetooth Special Interest Group, "Bluetooth core specification v5.1," 2019, accessed: 2025-4-8. [Online]. Available: https://www.bluetooth.com/specifications/specs/core-specification-amended-5-1/

[16] C. Huang, Y. Zhuang, H. Liu, J. Li, and W. Wang, "A performance evaluation framework for direction finding using BLE AoA/AoD receivers," *IEEE Internet Things J.*, vol. 8, no. 5, pp. 3331–3345, Mar. 2021.

[17] D. Sun *et al.*, "A BLE indoor positioning algorithm based on weighted fingerprint feature matching using AOA and RSSI," in *13th Int. Conf. Wireless Commun. Signal Process. (WCSP)*, Changsha, China, Oct. 2021, pp. 1–6.

[18] X. Hou and J. Bergmann, "Pedestrian dead reckoning with wearable sensors: A systematic review," *IEEE Sensors J.*, vol. 21, no. 1, pp. 143–152, Jan. 2021.

[19] Z. Zhu, Y. Yang, M. Chen, C. Guo, J. Cheng, and S. Cui, "A survey on indoor visible light positioning systems: Fundamentals, applications, and challenges," *IEEE Commun. Surv. Tut.*, early access, Oct. 1, 2024.

[20] X. Du, X. Liao, Z. Gao, and Y. Fan, "An enhanced particle filter algorithm with map information for indoor positioning system," in *IEEE Glob. Commun. Conf. (GLOBECOM)*, Waikoloa, HI, USA, Dec. 2019, pp. 1–6.

[21] S. Xu *et al.*, "Bluetooth, floor-plan, and microelectromechanical systems-assisted wide-area audio indoor localization system: Apply to smartphones," *IEEE Trans. Ind. Electron.*, vol. 69, no. 11, pp. 11 744–11 754, Nov. 2022.

[22] T.-M. T. Dinh, N.-S. Duong, and Q.-T. Nguyen, "Developing a novel real-time indoor positioning system based on BLE beacons and smartphone sensors," *IEEE Sensors J.*, vol. 21, no. 20, pp. 23 055–23 068, Oct. 2021.

[23] A. Poulose, O. S. Eyobu, and D. S. Han, "A combined PDR and Wi-Fi trilateration algorithm for indoor localization," in *Int Conf. Artif. Intell. Inf. Commun. (ICAIIC)*, Okinawa, Japan, Feb. 2019, pp. 72–77.

[24] J. Sun, X. Yu, D. Liu, Y. Zhai, and C. Wang, "Research on indoor location technology based on the fusion of WiFi and PDR," in *13th Int. Conf. Intell. Comput. Technol. Automat. (ICICTA)*, Xi'an, China, Oct. 2020, pp. 416–419.

[25] Y. Liu, C. Wu, X. Kong, X. Du, and Y. You, "A tightly coupled method for indoor vehicle navigation based on smartphone IMU and BLE," *IEEE Trans. Instrum. Meas.*, vol. 73, 2024, Art. no. 8509612.

[26] X. Kong, C. Wu, Y. You, and Y. Yuan, "Hybrid indoor positioning method of BLE and PDR based on adaptive feedback EKF with low BLE deployment density," *IEEE Trans. Instrum. Meas.*, vol. 72, 2023, Art. no. 9500912.

[27] H. Yu *et al.*, "Floor-plan-aided indoor localization: Zero-shot learning framework, data sets, and prototype," *IEEE J. Sel. Areas Commun.*, vol. 42, no. 9, pp. 2472–2486, Sept. 2024.

[28] W. Chai, C. Li, and Q. Li, "Multi-sensor fusion-based indoor single-track semantic map construction and localization," *IEEE Sensors J.*, vol. 23, no. 3, pp. 2470–2480, Feb. 2023.

[29] L. Huang *et al.*, "HPIPS: A high-precision indoor pedestrian positioning system fusing WiFi-RTT, MEMS, and map information," *Sensors*, vol. 20, no. 23, 2020, Art. no. 6795.

[30] X. Guo, N. Ansari, F. Hu, Y. Shao, N. R. Elikplim, and L. Li, "A survey on fusion-based indoor positioning," *IEEE Commun. Surv. Tut.*, vol. 22, no. 1, pp. 566–594, 1st Quart. 2020.

[31] X. Sui, J. Song, C. Wang, W. Ding, S. Gao, and Z. Shi, "UWB/MEMS IMU integrated positioning method based on NLOS angle discrimination and MAP constraints," *Sci. Rep.*, vol. 14, 2024, Art. no. 19879.

[32] H. Nurminen, M. Raitoharju, and R. Piché, "An efficient indoor positioning particle filter using a floor-plan based proposal distribution," in *19th Int. Conf. Inf. Fusion (FUSION)*, Heidelberg, Germany, Jul. 2016, pp. 541–548.

[33] H. Xia, J. Zuo, S. Liu, and Y. Qiao, "Indoor localization on smartphones using built-in sensors and map constraints," *IEEE Trans. Instrum. Meas.*, vol. 68, no. 4, pp. 1189–1198, Apr. 2019.

[34] M. Sun, Y. Wang, Q. Wang, G. Chen, and Z. Li, "Smartphone-based WiFi RTT/RSS/PDR/map indoor positioning system using particle filter," *IEEE Trans. Instrum. Meas.*, vol. 74, 2025, Art. no. 9501115.

[35] Y. Lin and K. Yu, "An improved integrated indoor positioning algorithm based on PDR and Wi-Fi under map constraints," *IEEE Sensors J.*, vol. 24, no. 15, pp. 24 096–24 107, Aug. 2024.

[36] A. Perttula, H. Leppäkoski, M. Kirkko-Jaakkola, P. Davidson, J. Collin, and J. Takala, "Distributed indoor positioning system with inertial measurements and map matching," *IEEE Trans. Instrum. Meas.*, vol. 63, no. 11, pp. 2682–2695, Nov. 2014.

[37] X. Wang, M. Jiang, Z. Guo, N. Hu, Z. Sun, and J. Liu, "An indoor positioning method for smartphones using landmarks and PDR," *Sensors*, vol. 16, no. 12, 2016, Art. no. 2135.

[38] J. Choi, G. Lee, S. Choi, and S. Bahk, "Smartphone based indoor path estimation and localization without human intervention," *IEEE Trans. Mob. Comput.*, vol. 21, no. 2, pp. 681–695, Feb. 2022.

[39] S. Xu, R. Chen, Y. Yu, G. Guo, and L. Huang, "Locating smartphones indoors using built-in sensors and Wi-Fi ranging with an enhanced particle filter," *IEEE Access*, vol. 7, pp. 95 140–95 153, 2019.

[40] P. Bahl and V. Padmanabhan, "RADAR: An in-building RF-based user location and tracking system," in *Proc. IEEE Conf. Comput. Commun. (INFOCOM)*, vol. 2, Tel Aviv, Israel, Mar. 2000, pp. 775–784.

[41] W. Pan, Y. Yang, Y. Nie, and Z. Ghassemlooy, "LED detection and occlusion compensation method for robust visible light positioning," in *14th Int. Symp. Commun. Syst. Netw. Digit. Signal Process. (CSNDSP)*, Rome, Italy, Jul. 2024, pp. 65–69.

[42] L. Vincent, "Morphological grayscale reconstruction in image analysis: applications and efficient algorithms," *IEEE Trans. Image Process.*, vol. 2, no. 2, pp. 176–201, Apr. 1993.

[43] Android Developers, "Sensors and location: Sensors overview," 2025, accessed: 2025-4-8. [Online]. Available: https://developer.android.com/develop/sensors-and-location/sensors/sensors_overview?hl=en

[44] H. Weinberg, *AN-602 Application Note: Using the ADXL202 in pedometer and personal navigation applications*, Analog Devices Inc., Norwood, MA, USA, 2002.

[45] S. O. H. Madgwick, A. J. L. Harrison, and R. Vaidyanathan, "Estimation of IMU and MARG orientation using a gradient descent algorithm," in *IEEE Int. Conf. Rehabil. Robot. (ICORR)*, Zurich, Switzerland, Jun. 2011, pp. 1–7.

[46] R. Douc and O. Cappe, "Comparison of resampling schemes for particle filtering," in *Proc. 4th Int. Symp. Image Signal Process. Anal. (ISPA)*, Zagreb, Croatia, Sept. 2005, pp. 64–69.

[47] L. Alsmadi, X. Kong, K. Sandrasegaran, and G. Fang, "An improved indoor positioning accuracy using filtered RSSI and beacon weight," *IEEE Sensors J.*, vol. 21, no. 16, pp. 18 205–18 213, Aug. 2021.

[48] Z. Jin, Y. Li, Z. Yang, Y. Zhang, and Z. Cheng, "Real-time indoor positioning based on BLE beacons and pedestrian dead reckoning for smartphones," *Appl. Sci.*, vol. 13, no. 7, 2023, Art. no. 4415.